(Supplementary Material)
Blur Aware Calibration of Multi-Focus Plenoptic Camera

Mathieu Labussière[1], Céline Teulière[1], Frédéric Bernardin[2], Omar Ait-Aider[1]

[1] Université Clermont Auvergne, CNRS, SIGMA Clermont,
Institut Pascal, F-63000 Clermont-Ferrand, France

[2] Cerema, Équipe-projet STI, 10 rue Bernard Palissy, F-63017 Clermont-Ferrand, France

mathieu.labu@gmail.com, firstname.name@{uca,cerema}.fr

As supplementary material, we first provide details about the camera model, second we detail in a more complete fashion the equations for the micro-image (MI) radii computation, third we complete the calibration results with the previously omitted parameters, and finally we give insight about the dataset images and poses.

A. Camera model

For completeness, the notations used in this paper are summarized in Fig. 1.

A.1. Main lens distortions

Recall that in our model, only distortions of the main lens are considered. Distortions represent deviations from the theoretical thin lens projection model. To correct those errors, we can undistort a distorted point $\boldsymbol{p} = \begin{bmatrix} x & y & z \end{bmatrix}^\top$ by applying a function φ to it, such as $\boldsymbol{p} \xrightarrow{\varphi} \boldsymbol{p}_u$. To model the radial $\varphi^{(r)}$ and tangential $\varphi^{(t)}$ components of the lateral distortion model, we use the model of Brown-Conrady [1, 2]. The radial component is thus expressed as

$$\begin{cases} x_u^{(r)} = x \cdot (1 + A_0\kappa^2 + A_1\kappa^4 + A_2\kappa^6) \\ y_u^{(r)} = y \cdot (1 + A_0\kappa^2 + A_1\kappa^4 + A_2\kappa^6), \end{cases} \tag{1}$$

and the tangential component as

$$\begin{cases} x_u^{(t)} = B_0(\kappa^2 + 2x^2) + 2B_1 xy \\ y_u^{(t)} = B_1(\kappa^2 + 2y^2) + 2B_0 xy, \end{cases} \tag{2}$$

where $\kappa = \sqrt{x^2 + y^2}$.

Finally, our set of intrinsic Ξ includes 5 lateral distortion parameters: three coefficients for the radial component, $\boldsymbol{k}^{(r)} = \{A_0, A_1, A_2\}$, and two for the tangential, $\boldsymbol{k}^{(t)} = \{B_0, B_1\}$.

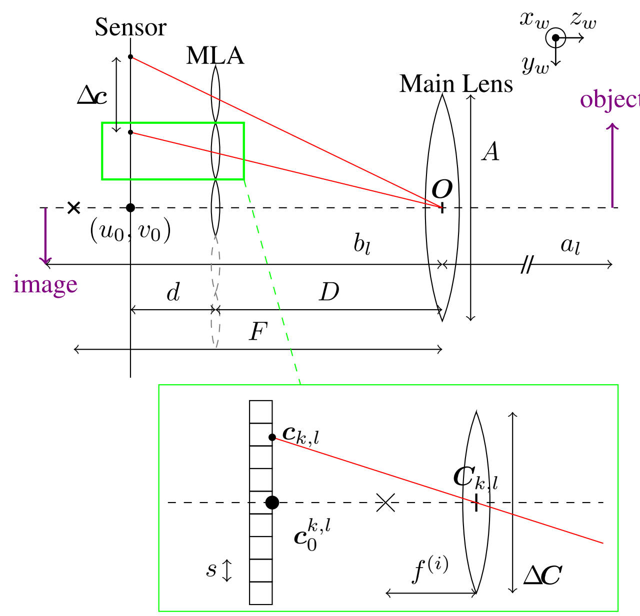

Figure 1: Focused Plenoptic Camera model in Galilean configuration (*i.e.*, the main lens focuses behind the sensor) with the notations used in this paper. Pixel counterparts of metric values are denoted in lower-case Greek letters.

A.2. F-number matching principle

The f-number of an optical system is the ratio between the system's focal length F and the diameter of the entrance pupil, A, given by

$$N = \frac{F}{A}. \tag{3}$$

The f-number accurately describes the light-gathering ability of a lens only for objects an infinite distance away. In optical design, an alternative is often needed for systems where the object is not far from the lens. In these cases the working f-number is used. The working f-number is defined as

$$N^{*} \approx \frac{1}{2\mathrm{NA}} \approx (1+|\gamma|)\, N, \tag{4}$$

where NA is the numerical aperture, *i.e.*, the number that characterizes the range of angles over which the system can accept or emit light, and γ is the magnification of the current focus setting. Let a be the quantity that verifies the following thin lens equation:

$$\frac{1}{F} = \frac{1}{a} + \frac{1}{D}, \tag{5}$$

where F is the focal length and D is the distance between the sensor and the lens. Then we can express the magnification as

$$\gamma = \frac{D}{a}, \tag{6}$$

and thus we can rearrange Eq. (3) and Eq. (4) to obtain the working f-number expressed as:

$$N^{*} = \left(1+\frac{D}{a}\right)\frac{F}{A} = D\left(\frac{1}{D}+\frac{1}{a}\right)\frac{F}{A} = \frac{D}{A}. \tag{7}$$

The fundamental design principle for light-field imaging is that the working f-numbers of the micro-lenses and the main lens are matched. This condition maximizes the fill factor of the sensor while avoiding overlap between micro-images [3]. Both unfocused and focused plenoptic camera designs follow the f-number matching principle. As highlighted in [5], the micro images generated by the micro-lenses in a plenoptic camera should just touch to make the best use of the image sensor, meaning

$$\frac{d}{\Delta C} = \frac{D_s - d}{A} \Longleftrightarrow N_{\mu}^{*} = N_{l}^{*} - \frac{d}{A}, \tag{8}$$

where d is the distance between the Micro-Lenses Array (MLA) and the sensor, $D_s = D + d$ is the distance between the main lens and the sensor, ΔC and A are respectively the diameters of the micro-lenses and the main lens, and, N_{μ}^{*} and N_{l}^{*} are respectively the working f-numbers of the micro-lenses and the main lens.

Since typically $d \ll A$, we have $N_{\mu}^{*} \approx N_{l}^{*}$. So, the working f-numbers of the main imaging system and the micro lens imaging system should match. This also implies that the design of the micro lenses fixes the f-number of the main lens that is used with the plenoptic camera.

A.3. Projection model

The blur aware plenoptic projection matrix $\boldsymbol{\mathcal{P}}(i,k,l)$ through the micro-lens (k,l) of type i is computed as

$$\begin{aligned}
\boldsymbol{\mathcal{P}}(i,k,l) &= \boldsymbol{P}(k,l)\cdot \boldsymbol{K}\left(f^{(i)}\right) \\
&= \begin{bmatrix} d/s & 0 & u_0^{k,l} & 0 \\ 0 & d/s & v_0^{k,l} & 0 \\ 0 & 0 & s\frac{\Delta C}{2} & -s\frac{\Delta C}{2}d \\ 0 & 0 & -1 & 0 \end{bmatrix}
\begin{bmatrix} 1 & 0 & 0 & 0 \\ 0 & 1 & 0 & 0 \\ 0 & 0 & 1 & 0 \\ 0 & 0 & -1/f^{(i)} & 1 \end{bmatrix} \\
&= \begin{bmatrix} d/s & 0 & u_0^{k,l} & 0 \\ 0 & d/s & v_0^{k,l} & 0 \\ 0 & 0 & s\frac{\Delta C}{2}d\left(\frac{1}{d}-\frac{1}{f^{(i)}}\right) & -s\frac{\Delta C}{2}d \\ 0 & 0 & -1 & 0 \end{bmatrix},
\end{aligned} \tag{9}$$

where d is the distance between the MLA and the sensor, s is the size of a pixel, $\boldsymbol{c}_0^{k,l} = \begin{bmatrix} u_0^{k,l} & v_0^{k,l} \end{bmatrix}^{\top}$ is the principal point of the micro-lens (k,l), ΔC is the diameter of the micro-lens, and $f^{(i)}$ is the micro-lens focal length.

B. Micro-image radii computation

B.1. Image moments fitting

From raw white images, we measure each micro-image (MI) radius $\varrho = |R|/s$ in pixel based on image moments fitting. We use the second order central moments of the micro-image to construct a covariance matrix. Raw moments and centroid are given by

$$M_{ij} = \sum_{x,y} x^i y^j \mathcal{I}(x,y) \quad \text{and} \quad \{\bar{x},\ \bar{y}\} = \left\{\frac{M_{10}}{M_{00}}, \frac{M_{01}}{M_{00}}\right\},$$

and the central moments are given by

$$\mu_{pq} = \sum_{x,y} (x-\bar{x})^p (y-\bar{y})^q \mathcal{I}(x,y). \tag{10}$$

The covariance matrix is then given by

$$\operatorname{cov}[\mathcal{I}(x,y)] = \frac{1}{\mu_{00}}\begin{bmatrix} \mu_{20} & \mu_{11} \\ \mu_{11} & \mu_{02} \end{bmatrix} = \begin{bmatrix} \sigma_{xx} & \sigma_{xy} \\ \sigma_{yx} & \sigma_{yy} \end{bmatrix}. \tag{11}$$

We choose σ as the square root of the greater eigenvalue of the covariance matrix, *i.e.*,

$$\sigma^2 = \lambda_{\max} = \frac{\sigma_{xx}+\sigma_{yy}}{2} + \frac{\sqrt{4\sigma_{xy}^2 + (\sigma_{xx}-\sigma_{yy})^2}}{2}. \tag{12}$$

Finally, the radius ϱ is proportional to the computed standard deviation σ.

Type	$N = 5.66$	$N = 8$	$N = 11.31$
$i = 1$	56.79±0.56	47.08±0.53	42.76±1.04
$i = 2$	53.68±0.95	41.71±0.78	35.68±1.36
$i = 3$	56.58±0.91	44.46±0.73	38.98±1.32

Table 1: Statistics (mean±std) over radii measurements (in µm) for each type of micro-image at different apertures.

B.2. Radii distribution analysis

An analysis of the micro-image radii distribution is given for three apertures $N \in \{5.66, 8, 11.31\}$ in Tab. 1 for the dataset R12-A.

As expected, the radius decreases whilst the f-number N increases. The standard deviation is less than one-fifth of a pixel, meaning that our method provides precise results.

B.3. Coefficients estimation

From radii measurements at different f-numbers, we want to estimate the coefficients $\boldsymbol{X} = \begin{bmatrix} m & q_1 & \dots & q_I \end{bmatrix}^\top$ of

$$\mathrm{R}\left(N^{-1}\right) = m \cdot N^{-1} + q_i \tag{13}$$

with

$$m = \frac{dF}{2D} \quad \text{and} \quad q_i = \frac{1}{f^{(i)}} \cdot \left(\frac{\Delta c D}{d + D}\right) \cdot \frac{d}{2} - \frac{\Delta c}{2}. \tag{14}$$

Note that m is a function of fixed physical parameters independent of the micro-lenses focal lengths and the main lens aperture. Therefore, we obtain a set of linear equations, sharing the same slope, but with different y-intercepts. This set of equations can be rewritten as

$$\boldsymbol{A}\boldsymbol{X} = \boldsymbol{B}, \text{ and then } \boldsymbol{X} = \left(\boldsymbol{A}^\top \boldsymbol{A}\right)^{-1} \boldsymbol{A}^\top \boldsymbol{B}$$

where the matrix $\boldsymbol{A}$ (containing the f-numbers and a selector of the corresponding y-intercept coefficient) and $\boldsymbol{B}$ (containing the radii measurements) are constructed by arranging the terms given the focal length at which they have been calculated. Finally, we compute $\boldsymbol{X}$ with a least-square estimation.

C. Supplements on calibration results

Some parameters have been omitted in the main paper for compactness. Tab. 2 presents the complete set of intrinsic parameters with their initial and optimized values for our method and compared to [4]. As stated, the distortions coefficients are really low, and the MLA rotations are negligible. Indeed, in the case of industrial plenoptic cameras, such as `Raytrix` ones, a careful attention is payed to the co-planarity of the MLA and the sensor plane.

D. Insight about the datasets

We have presented three datasets in the submitted work: R12-A, R12-B, and R12-C. The devignetted images of the calibration targets from the dataset R12-A (Fig. 2), R12-B (Fig. 4), and R12-C (Fig. 6) taken at various angles and distances are presented below along with the poses at which they have been taken (Fig. 3, Fig. 5, and Fig. 7).

D.1. Software and setup

All images has been acquired using the free software `MultiCam Studio` (v6.15.1.3573) of the company `Euresys`. The shutter speed has been set to 5 ms. While taking white images for the pre-calibration step, the gain has been set to its maximum value. For `Raytrix` data, we use their proprietary software `RxLive` (v4.0.50.2) to calibrate the camera, and compute the depth maps used in the evaluation.

D.2. Dataset R12-A

The dataset has been taken at short focus distance, $h = 450$ mm. Therefore, the checkerboard squares size had to be decreased to 10 mm so we can observe the corner in image space. All the poses have been acquired at distances between 400 and 175 mm from the checkerboard.

Controlled evaluation. The dataset is composed of 11 poses taken with a relative step of 10 mm between each pose along the z-axis direction, at distances between 385 and 265 mm.

D.3. Dataset R12-B

The dataset has been taken at middle focus distance, $h = 1000$ mm. Therefore, the checkerboard squares size is set to 20 mm so we can observe the corner in image space. All the poses have been acquired at distances between 775 and 400 mm from the checkerboard.

Controlled evaluation. The dataset is composed of 10 poses taken with a relative step of 50 mm between each pose along the z-axis direction, at distances between 900 and 450 mm.

D.4. Dataset R12-C

The dataset has been taken at long focus distance, $h = \infty$. Therefore, the checkerboard squares size had to be increased to 30mm so we can observe the corner in image space. All the poses have been acquired at distances between 2500 and 500 mm from the checkerboard.

Controlled evaluation. The dataset is composed of 18 poses taken with a relative step of 50 mm between each pose along the z-axis direction, at distances between 1250 and 400 mm.

		R12-A ($h = 450$mm)			R12-B ($h = 1000$mm)			R12-C ($h = \infty$)		
	Unit	Initial	Ours	[4]	Initial	Ours	[4]	Initial	Ours	[4]
F	[mm]	50	49.720	54.888	50	50.047	51.262	50	50.011	53.322
A_0	[$\times 10^{-5}$]	0	23.145	6.099	0	1.686	0.023	0	18.647	1.393
$-A_1$	[$\times 10^{-6}$]	0	2.934	0.925	0	0.177	0.093	0	2.652	0.382
A_2	[$\times 10^{-8}$]	0	1.078	0.303	0	0.023	0.007	0	1.036	0.104
B_0	[$\times 10^{-5}$]	0	-9.870	-15.028	0	14.373	12.143	0	18.971	27.720
$-B_1$	[$\times 10^{-5}$]	0	5.387	5.020	0	18.947	18.164	0	7.600	4.461
D	[mm]	56.658	56.696	62.425	52.113	52.125	53.296	49.384	49.384	52.379
$-t_x$	[mm]	11.293	11.129	9.771	11.299	12.503	12.672	11.302	13.213	14.159
$-t_y$	[mm]	8.411	8.186	8.334	8.416	6.305	6.114	8.418	7.256	6.231
$-\theta_x$	[µrad]	0	875.200	468.600	0	648.400	576.200	0	575.100	487.700
θ_y	[µrad]	0	669.700	321.800	0	417.400	350.400	0	445.600	366.100
θ_z	[µrad]	0.553	30.100	25.300	16.989	36.600	35.300	27.961	44.500	49.100
ΔC	[µm]	127.51	127.45	127.38	127.47	127.45	127.40	127.54	127.50	127.42
$f^{(1)}$	[µm]	578.15	577.97	-	581.10	580.48	-	554.35	556.09	-
$f^{(2)}$	[µm]	504.46	505.21	-	503.96	504.33	-	475.98	479.03	-
$f^{(3)}$	[µm]	551.67	551.79	-	546.39	546.37	-	518.98	521.33	-
u_0	[pix]	2039	2042.55	2289.83	2039	1790.94	1759.29	2039	1661.95	1487.2
v_0	[pix]	1533	1556.29	1528.24	1533	1900.19	1934.87	1533	1726.91	1913.81
d	[µm]	318.63	325.24	402.32	336.84	336.26	363.17	307.93	312.62	367.40

Table 2: Initial intrinsic parameters for each dataset along with the optimized parameters obtained by our method and with the method of [4].

E. Source code and datasets redistribution

The datasets and the source code are publicly available to the community. Datasets can be downloaded from `https://github.com/comsee-research/plenoptic-datasets`.
We also developed an open-source C++ library for plenoptic camera named `libpleno` which is available at `https://github.com/comsee-research/libpleno`.
Along with this library, we developed a set of tools to pre-calibrate and calibrate a multifocus plenoptic camera, named `COMPOTE` (standing for Calibration Of Multifocus PlenOpTic camEra) which is available at `https://github.com/comsee-research/compote`.

Acknowledgments

This work has been sponsored by the AURA Region and the European Union (FEDER) through the MMII project of CPER 2015-2020 MMaSyF challenge. We thank Charles-Antoine Noury and Adrien Coly for their insightful discussions and their help during the acquisitions.

References

[1] Duane Brown. Decentering Distortion of Lenses - The Prism Effect Encountered in Metric Cameras can be Overcome Through Analytic Calibration. *Photometric Engineering*, 32(3):444–462, 1966. 1

[2] Ae Conrady. Decentered Lens-Systems. *Monthly Notices of the Royal Astronomical Soceity*, 79:384–390, 1919. 1

[3] Ren Ng, Marc Levoy, Gene Duval, Mark Horowitz, and Pat Hanrahan. Light Field Photography with a Hand-held Plenoptic Camera. Technical report, Stanford University, 2005. 2

[4] Charles Antoine Noury, Céline Teulière, and Michel Dhome. Light-Field Camera Calibration from Raw Images. *DICTA 2017 – International Conference on Digital Image Computing: Techniques and Applications*, pages 1–8, 2017. 3, 4

[5] Christian Perwaß and Lennart Wietzke. Single Lens 3D-Camera with Extended Depth-of-Field. In *Human Vision and Electronic Imaging XVII*, volume 49, page 829108. SPIE, feb 2012. 2

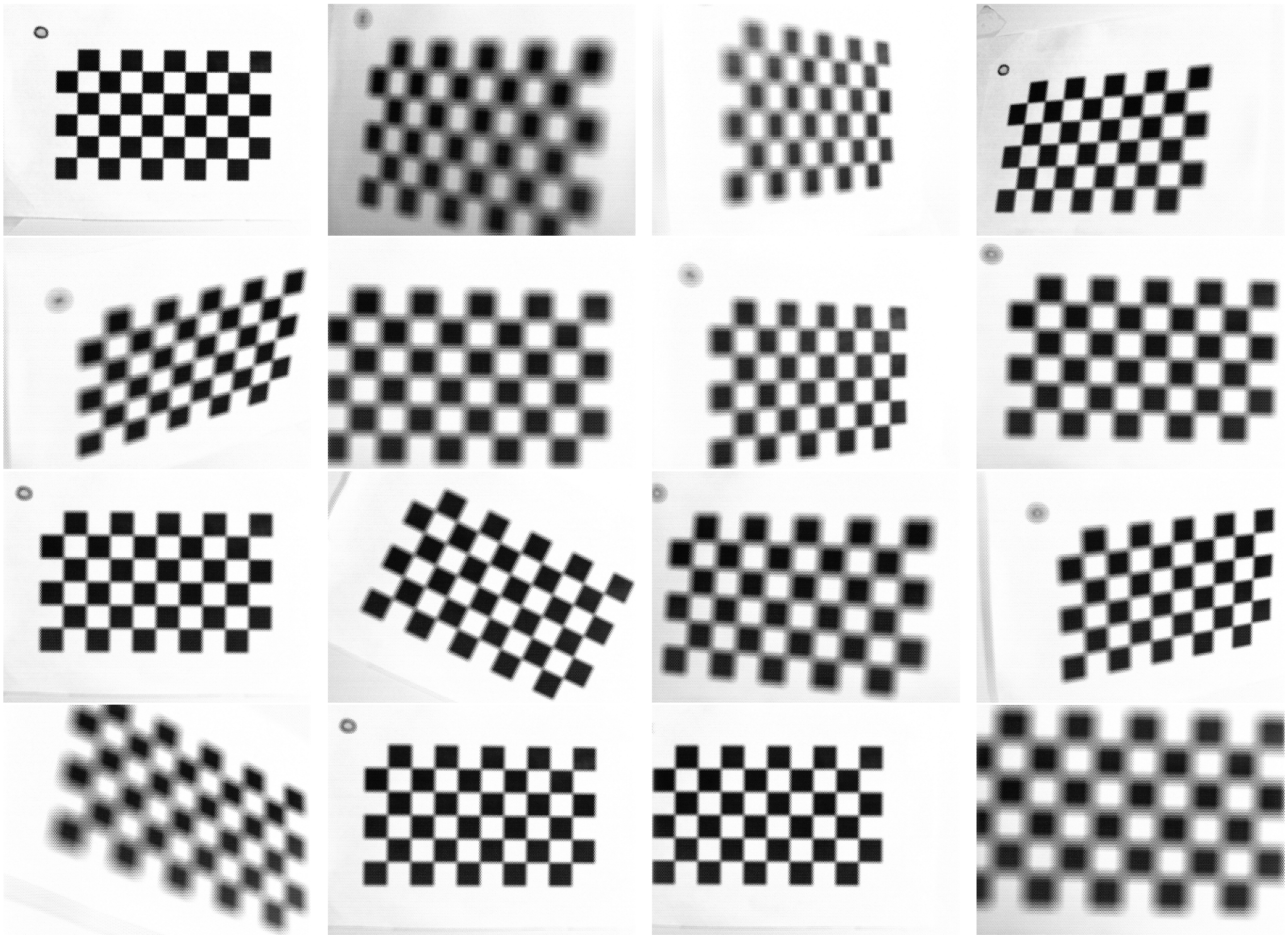

Figure 2: Devignetted images of the calibration targets (9×5 of $10\mathrm{mm}$ side checkerboard) from the dataset R12-A taken at various angles and distances.

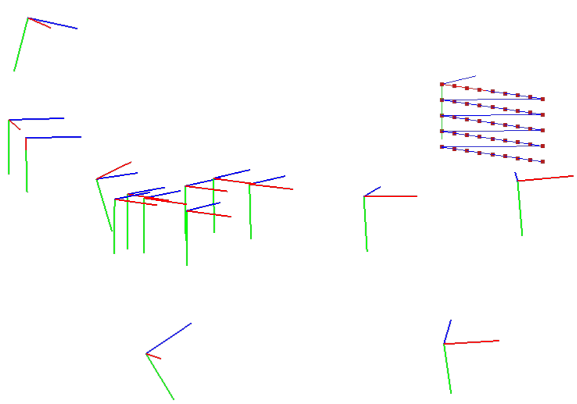

Figure 3: Poses of the camera while capturing the calibration targets from dataset R12-A.

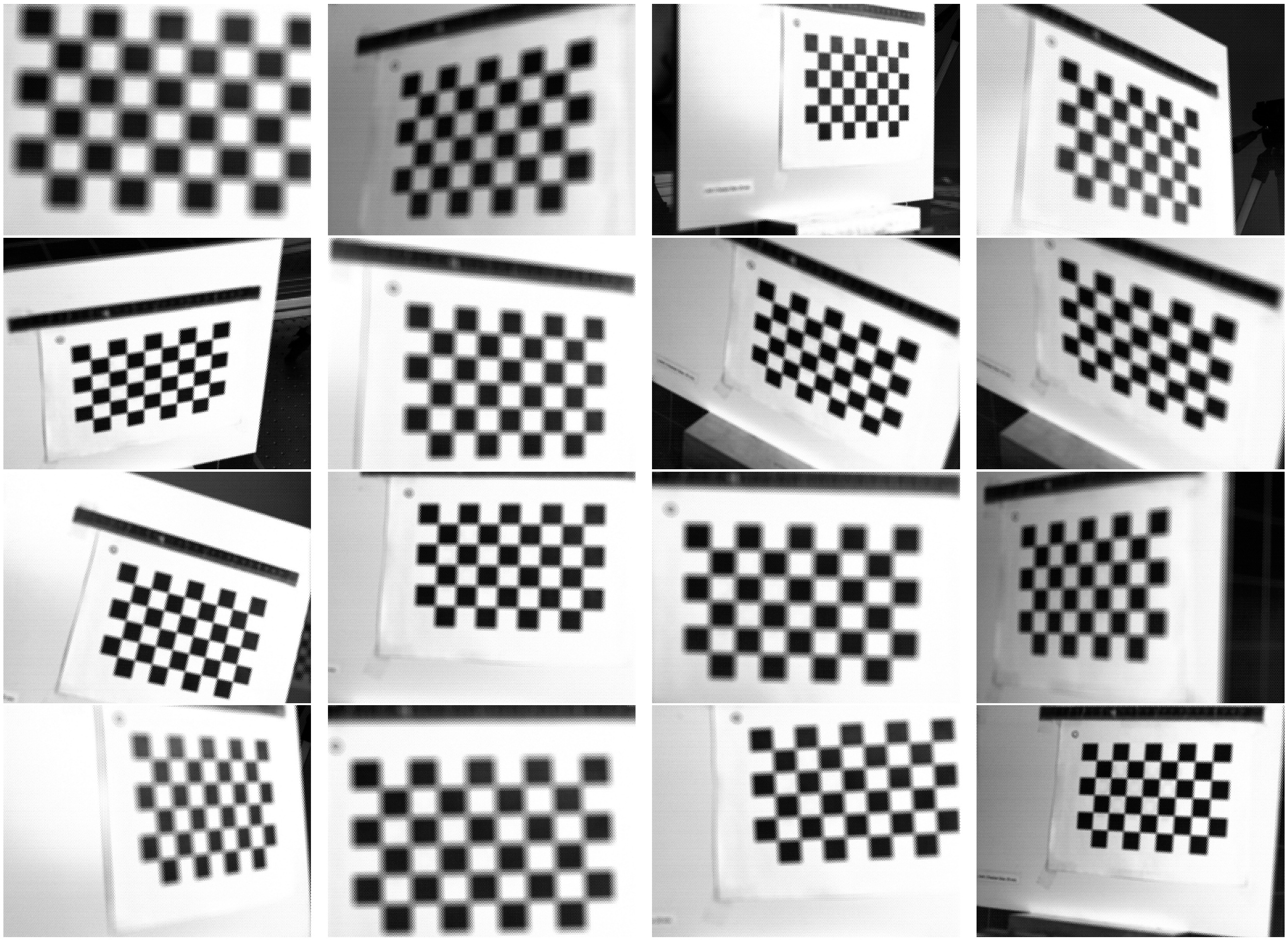

Figure 4: Devignetted images of the calibration targets (8×5 of $20\mathrm{mm}$ side checkerboard) from the dataset R12-B taken at various angles and distances.

Figure 5: Poses of the camera while capturing the calibration targets from dataset R12-B.

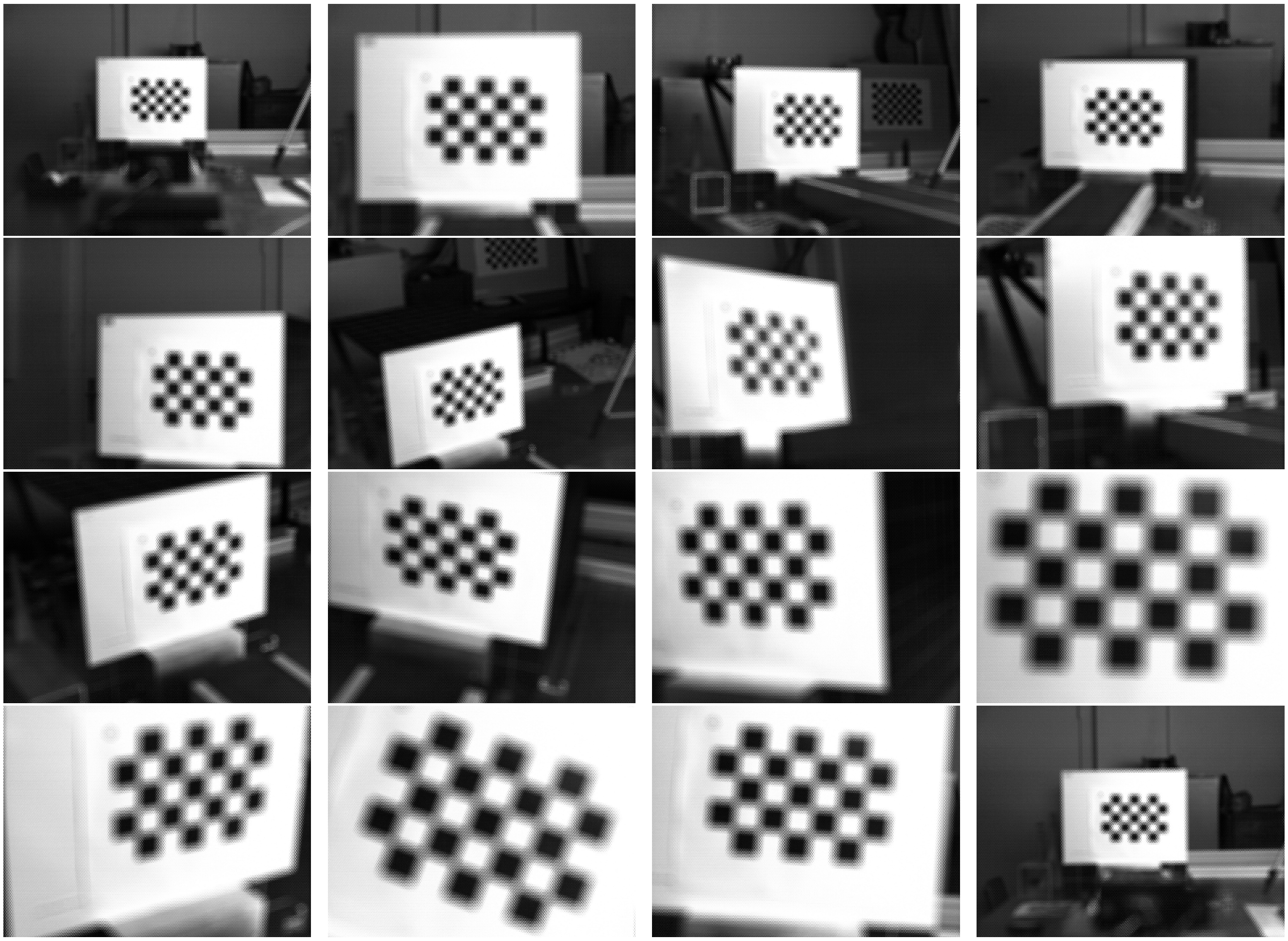

Figure 6: Devignetted images of the calibration targets (7×5 of 30mm side checkerboard) from the dataset R12-C taken at various angles and distances.

Figure 7: Poses of the camera while capturing the calibration targets from dataset R12-C.